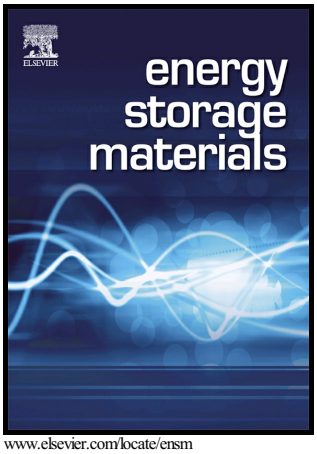

www.elsevier.com/locate/ensm

Controlled synthesis of anisotropic hollow $ZnCo_2O_4$ octahedrons for high-performance lithium storage

Jiaojiao Deng, Xiaoliang Yu, Xianying Qin, Bilu Liu, Yan-Bing He, Baohua Li, Feiyu Kang

PII: S2405-8297(17)30144-7
DOI: http://dx.doi.org/10.1016/j.ensm.2017.06.014
Reference: ENSM174

To appear in: *Energy Storage Materials*

Received date: 17 April 2017
Revised date: 13 June 2017
Accepted date: 25 June 2017

Cite this article as: Jiaojiao Deng, Xiaoliang Yu, Xianying Qin, Bilu Liu, Yan-Bing He, Baohua Li and Feiyu Kang, Controlled synthesis of anisotropic hollow $ZnCo_2O_4$ octahedrons for high-performance lithium storage, *Energy Storage Materials,* http://dx.doi.org/10.1016/j.ensm.2017.06.014

Controlled synthesis of anisotropic hollow $ZnCo_2O_4$ octahedrons for high-performance lithium storage

Jiaojiao Deng [a,b‡], Xiaoliang Yu [d‡], Xianying Qin [a], Bilu Liu [c], Yan-Bing He [a], Baohua Li [a,*], Feiyu Kang [a,b]

[a]Engineering Laboratory for Next Generation Power and Energy Storage Batteries, and Engineering Laboratory for Functionalized Carbon Materials, Graduate School at Shenzhen, Tsinghua University, Shenzhen 518055, China

[b]School of Materials Science and Engineering, Tsinghua University, Beijing 100084, China

[c]Tsinghua-Berkeley Shenzhen Institute (TBSI), Tsinghua University, Shenzhen 518055, China

[d]National Institute for Materials Science, 1-2-1 Sengen, Tsukuba 305-0047, Japan

libh@tsinghua.edu.cn (B. Li).

Abstract

Hollow micro-/nanostructures of metal oxides have attracted tremendous research attention in energy storage due to their unique structural advantages. Although fabrication of spherical hollow architectures have been intensively reported, rational design and facile synthesis of anisotropic hollow structures are still quite challenging, especially for those complex mixed metal oxides with well-controlled interior structures. Herein, through facile citrate-assisted hydrothermal synthesis and subsequent controlled annealing, well-defined octahedral $ZnCo_2O_4$ solid, hollow and

yolk-shell micro-/nanostructures were constructed for the first time. When used as anode materials for lithium ion batteries (LIBs), the hollow $ZnCo_2O_4$ octahedron exhibits the best lithium storage properties, delivering high discharge capacities of 880 mA h g^{-1} over 160 cycles at 0.2 A g^{-1}, and 650 mA h g^{-1} over 300 cycles at 1 A g^{-1}. Moreover, it shows a superior high-rate performance with 60% of the specific capacity maintained even at a high current density of 5 A g^{-1}. These features render the hollow octahedral $ZnCo_2O_4$ micro-/nanostructure a promising anode for next generation LIBs.

Keywords: Ternary metal oxide; Anisotropic hollow structure; Hydrothermal synthesis; Lithium ion battery anode; High performance

Graphic Abstract

Well-defined octahedral $ZnCo_2O_4$ hollow micro-/nanostructure (H-ZCO) was constructed through citrate-assisted hydrothermal synthesis and subsequent controlled annealing process. When evaluated as lithium ion battery anode, it shows excellent electrochemical performances.

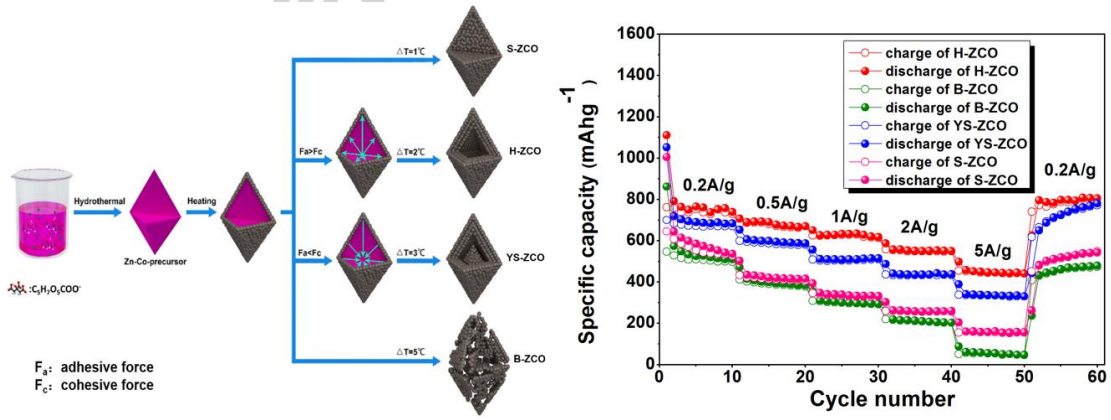

Introduction

The ever-growing demand for clean and sustainable energy has triggered considerable research on developing high performance energy storage devices. As one of the most promising power sources for portable electrical appliances and hybrid electric vehicles, rechargeable lithium-ion batteries (LIBs) have attracted worldwide attention due to their high energy density, high power capability, and long cycle life [1-5]. Nowadays the commercially used graphite anodes deliver quite low specific capacities of less than 370 mA h g^{-1}, which seriously hinders the wide application of LIBs, especially in electric vehicles [6, 7]. Therefore, it is highly desirable to exploit advanced high capacity anodes while maintaining good cycling stability and rate capability.

Among various candidates, $ZnCo_2O_4$, one typical kind of mixed metal oxides, has been widely recognized as a potential alternative electrode material to graphite. $ZnCo_2O_4$ can deliver a high specific capacity of ~900 mA h g^{-1} according to the multiple electrons transfer reaction: $ZnCo_2O_4+9Li^++9e^-\rightarrow ZnLi+2Co+4Li_2O$ [8, 9]. In addition, the synergetic effect between zinc and cobalt elements could improve electric/ionic conductivity as well as mechanical stability of $ZnCo_2O_4$, rendering it with improved electrochemical performance [10, 11]. However, the large volume changes of $ZnCo_2O_4$ during charge/discharge processes lead to fast capacity fading, which limits its practical application in LIBs [12]. To address above-mentioned issues, hollow micro-/nanostructures have been developed based on the following considerations [13, 14]. First, hollow structures can provide large electrode-electrolyte contact areas for more electrochemically active sites. Second, hollow architectures

can offer sufficient spaces to mitigate stresses resulting from drastic volume changes. Third, robust framework of microstructures can effectively alleviate prominent aggregation of nanosized primary particles [15-17].

Up to date, tremendous efforts have been devoted to developing various synthetic strategies for hollow architectures, including hard-template methods [18-20], soft-template methods [21-23], and self-template methods [24, 25]. Hollow architectures with different interior structures from single shell to yolk shell, even yolk multi-shell have been controllably fabricated through templating methods, including hollow Cu_2O, Co_3O_4, SnO_2, ZnO, etc [26-31].

Despite the great progresses achieved, the majority of research works focused on spherical hollow micro-/nanostructures. Considering anisotropic hollow structures can bring unique physical/chemical advantages that are difficult to achieve through traditional spherical structures [32], controlled synthesis of anisotropic hollow architectures is highly desirable. Nevertheless, the preparations are very difficult. First, conventional templating methods suffer from paucity of nonspherical templates and uneven coating on high-curvature template surfaces [33]. Second, nonspherical structures show poor shape preservation during thermal decomposition due to high residual stresses [34-36]. In this regard, appealing approaches based on different mechanisms such as Ostwald ripening [24], the Kirkendall effect [37], and galvanic replacement [25] have been used to fabricate various non-spherical hollow structures. These methods are very applicative for forming shells on high-curvature structures since the shell formation is caused by spontaneous chemical reaction, accompanied

with the removal of the templates. Another promising approach to synthesize hollow non-spherical structures is decomposition of certain solid state precursors. For instance, Huang et al. prepared Co_3O_4 hollow dodecahedra by thermal treatment of dodecahedrol zeolitic imidazolate framework (ZIF)-67 particles [35]. Similarly, Lou et al. utilized Prussian blue (PB) for synthesis of Fe_2O_3 hollow microboxes with various shell structures by controlled annealing process [33]. However, these above-mentioned strategies for creating anisotropic hollow structures could hardly be extended from binary metal oxides to ternary metal oxides (like $ZnCo_2O_4$) owing to the different chemical reactivity among different metal ions. Therefore, fabrication of anisotropic hollow structures of ternary metal oxides as high-performance LIB anodes may have great significances in materials science but still remains quite challenging.

In this research, we have developed a citrate-assisted hydrothermal synthesis and annealing method to prepare octahedral hollow $ZnCo_2O_4$ architectures. The advantages of this synthesis strategy includes: 1) As-obtained products show well-defined octahedral shape without any inward depression, 2) As-obtained products are highly crystalline spinel $ZnCo_2O_4$, 3) We realized controllable interior structure, including solid octahedron, hollow octahedron and yolk-shell octahedron by controlled annealing process, 4) The process is a facile, scalable, low-cost and eco-friendly synthesis method. When evaluated as LIBs anode materials, the hollow $ZnCo_2O_4$ octahedrons show excellent lithium storage properties.

1. Experimental

2.1 Materials synthesis

All the chemicals used in our experiments were of analytical grade and used as received. In a typical synthesis experiment, polyvinylpyrrolidone (PVP, 0.1g, Molecule weight is 58,000) was dissolved into distilled water (50 mL) under magnetic stirring. Subsequently, $Zn(Ac)_2 \cdot 2H_2O$ (1 mmol), $Co(Ac)_2 \cdot 4H_2O$ (2 mmol) and a certain amount of potassium citrate (ranging from 0 to 6 mmol) were added into the above solution. The resultant mixture was continually stirred and transferred into a Teflon lined stainless-steel autoclave (100 mL). Then the autoclave was heated to 180 ºC in 50 minutes and maintained for certain hours (0.5-20 hrs) before cooling down to room temperature. The as-prepared precursor was collected and washed with distilled water and absolute alcohol for several times, followed by drying at 80 °C for 12 hrs. Finally, octahedral $ZnCo_2O_4$ with different interior structures were obtained by annealing the precursors at 600 ºC for 4 hrs in air with various heating rates (ranging from 1 °C/min to 5 °C/min).

2.2 Structural characterization

The morphologies of as-prepared products were observed by scanning electron microscopy (SEM, ZEISS ULTRA55). The phases of the samples were characterized by powder X-ray diffraction (XRD, Rigaku D/max 2500/PC using Cu Kα radiation with λ = 1.5418 Å). Surface analysis of the sample was performed with an X-ray photoelectron spectroscopy (XPS). Porosity properties were tested by N_2 adsorption-desorption isotherm measurement at 77 K (Micromeritics ASAP 2020), and specific surface areas were calculated based on the Brunauer–Emmett–Teller (BET) method. The thermal stability of the samples was measured by

thermogravimetric (TGA, NETZSCH STA449F3) in air with a heating rate of 10 °C min^{-1}.

2.3 Electrochemical measurements

The CR2032-coin-type half cells were used to investigate the electrochemical performances of the synthesized $ZnCo_2O_4$ samples. To prepare working electrode, as-obtained $ZnCo_2O_4$, acetylene black, and polyvinylidene fluoride (PVDF) binder were mixed at a weight ratio of 7:2:1 in N-methyl-2-pyrolidinone. After stirring for 4 h, the slurry was coated onto a copper foil and dried under vacuum at 110 ºC for 12 h. The mass loading of active material on each electrode is about 1.1 mg cm^{-2}. Lithium foils were used as counter electrode. $LiPF_6$ (1 M) in a mixed solvent of ethylene carbonate (EC)/diethyl carbonate (DEC)/ethyl methyl carbonate (EMC) (volume ratio = 1: 1: 1) was used as the electrolyte. The galvanostatic charge/discharge tests were performed using a Land 2001A battery test system with a voltage window of 0.01–3.0 V at ambient temperature. Cyclic voltammetry (CV) was collected using a VMP3 electrochemical station at a scan rate of 0.1 mV s^{-1} in the potential range of 0.01–3.0 V. The electrochemical impedance spectroscopy (EIS) was also tested by the electrochemical workstation in a frequency range of 10 mHz to 100 kHz.

2. Results and discussion

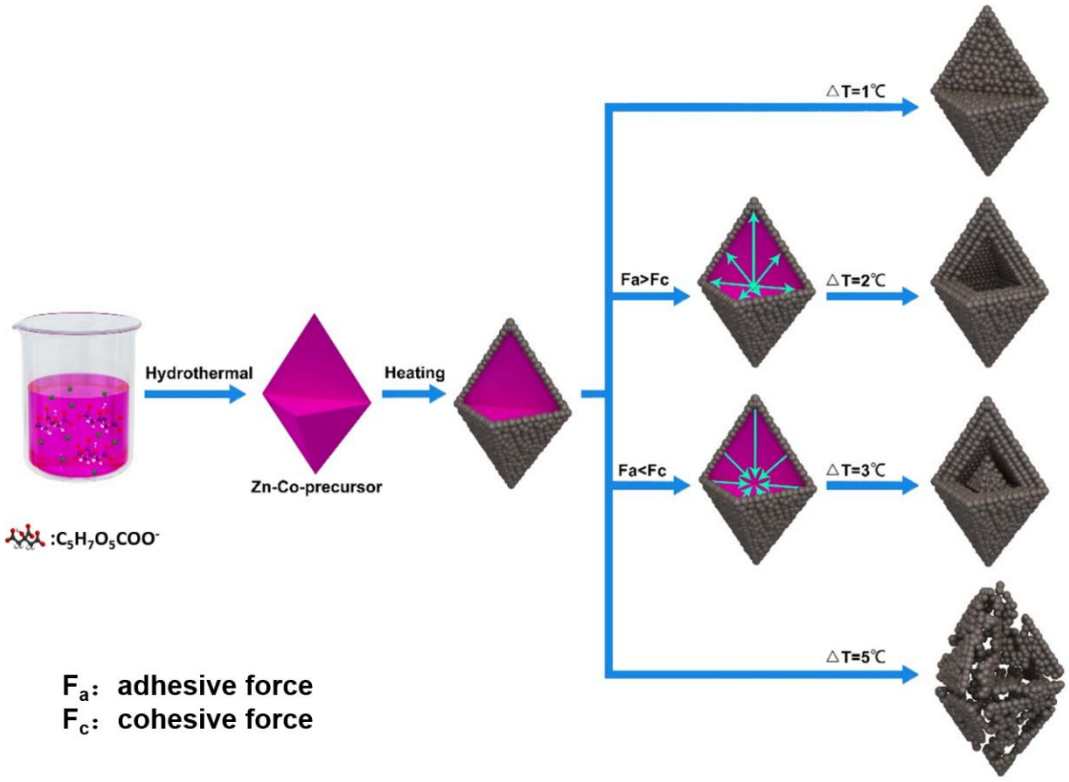

Scheme 1. Schematic illustration for the controlled synthesis of anisotropic hollow $ZnCo_2O_4$ octahedrons. Citrate assisted hydrothermal synthesis with appropriate citrate content and hydrothermal reaction time produces octahedral Zn-Co-precursor. Subsequent annealing process at ramping rates of 2 °C min^{-1} and 3 °C min^{-1} yields single-shell and yolk-shell hollow $ZnCo_2O_4$ octahedrons, respectively.

Scheme 1 illustrates formation process of $ZnCo_2O_4$ octahedrons with different interior structures. A hydrothermal synthesis was proposed to prepare the octahedral Zn-Co-precursor. The subsequent annealing process converted precursor into octahedral $ZnCo_2O_4$ with various interior structures, which could be generally divided to four types according to heterogeneous contraction process [38]. In the first type, which occurs at lower ramp rate, the Zn-Co-precursor are almost homogeneously

heated from the surface to center and finally shrink into solid porous structures. At a high ramp rate, there could be a large temperature gradient (ΔT) along the radial direction in the initial heating process, which leads to the formation of a $ZnCo_2O_4$ shell on the surface of octahedral Zn-Co-precursor. In the meantime, two forces from opposing directions would generate and exert on the interface between the $ZnCo_2O_4$ shell and the Zn-Co-precursor core. One is the cohesive force (F_c) from the inner core, which is induced by the weight loss of 46.2 % during the oxidative decomposition of inorganic substances, leading to the inward contraction of Zn-Co-pre core. The other is the adhesive force (F_a) originates from the relatively rigid shell, which resists shrinkage in the outer shell. When F_a surpasses F_c, the inner core is prone to diffuse into the $ZnCo_2O_4$ shell, leading to the formation of a hollow octahedral structure. When F_c is dominant, and the inner core will further contract inward and separate from the pre-formed outer metal oxide shell, producing a unique yolk-shell structure. For a higher heating rate, a large temperature gap between the surface and inner of octahedrons will generate, which gives rise to severe stress and leads to collapse of octahedral structure. As stated in Introduction section, the poor shape preservation of nonspherical Zn-Co-precursor during the annealing process is a big obstacle for fabricating anisotropic hollow architectures. Therefore, the key step for this synthesis strategy is the preparation of an appropriate Zn-Co-precursor. Potassium citrate was used as both hydrolysis accelerant and structure-directing agent. By careful controlling the citrate content and hydrothermal reaction time, the precursor with perfect octahedral morphology and good structural stability can be obtained and used

to fabricate well-defined hollow and yolk-shell octahedral architectures.

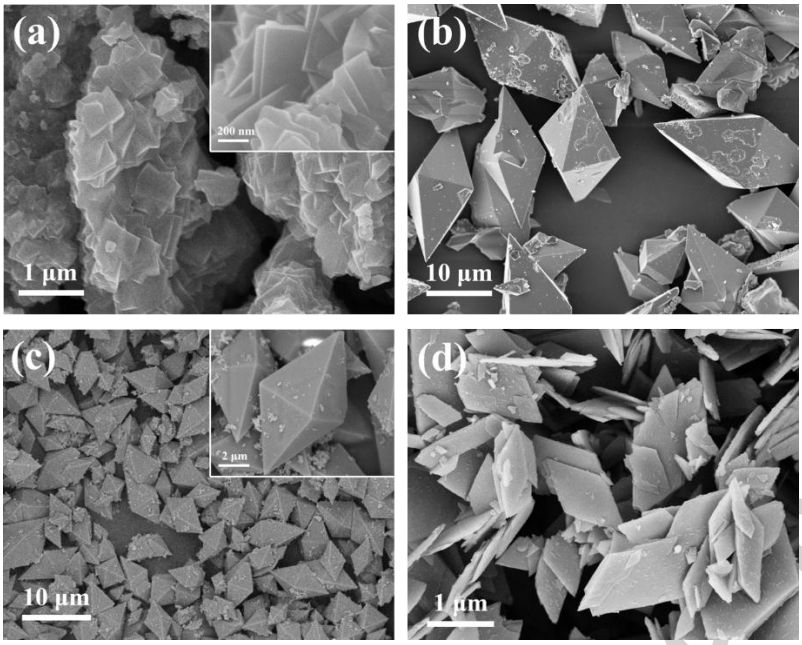

Fig. 1. SEM images of the hydrothermal products with different citrate contents: (a) Irregularly shaped particles obtained in the absence of citrate; (b) Large octahedrons formed with 1.5 mmol of citrate; (c) Well-defined octahedrons obtained in the presence of 3 mmol of citrate; (d) Diamond-shaped micro-sheets obtained with 4.5 mmol of citrate.

Citrate content plays an important role on the morphology of the hydrothermal products. Irregularly shaped particles constructed by closely stacked nanoplates were formed in the absence of potassium citrate (see Fig. 1a). When less potassium citrate (1.5 mmol) was used, the hydrothermal products were mainly octahedron-shaped particles. The surfaces are not so smooth and the particle sizes are in a wide range of 5 to 30 μm (Fig. 1b). In the presence of 3 mmol of potassium citrate, the products

exhibited well-defined octahedral morphology with small edge lengths (ranging from 5 to 10 μm, Fig. 1c). The solid internal structure of octahedron was clearly seen from the fracture surface of the grounded precursor (Fig. S1). On the other hand, increasing the amount of potassium citrate to 4.5 mmol resulted in the disappearance of octahedral particles and generation of diamond-shaped micro- sheets (Fig. 1d). These observations demonstrate that the appropriate of potassium citrate is vital to the formation of perfectly octahedron-shaped Zn-Co-precursor. Besides, we find that citrate content also has an effect on the yield of the Zn-Co-precursor. Table S1 shows the mass of products in this hydrothermal synthesis system with gradually increasing citrate content. When citrate was not used, only a small amount of hydrothermal product was formed. The quantity of precipitate increased gradually with the increase of citrate content and it reaches a maximum value of 488 mg when 3 mmol potassium citrate was used. As the citrate content further increased to 4.5 and 6 mmol, the yield decreased. This variation trend can be ascribed to two competitive reactions. On the one hand, citrates facilitate the hydrolysis of Zn^{2+} and Co^{2+} to form Zn-Co-precursor crystals. On the other hand, they can react with Zn^{2+} and Co^{2+} to form soluble metal chelates, which leads to the dissolution of crystals [39, 40]. Taking together, at an optimized citrate content of 3 mmol, highest yield hydrothermal product was achieved. Considering the well-defined octahedral morphology and highest yield, the hydrothermal product with potassium citrate of 3 mmol was chosen as the Zn-Co-precursor to prepare octahedral hollow $ZnCo_2O_4$ architectures.

We next conducted time-dependent experiments to evaluate the morphological

evolutions of octahedral Zn-Co-precursor in the present system. Detailed investigations elucidated the formation of octahedral precursor is through three steps, 1) nucleation, 2) nanocrystal self-assembly and octahedron formation, and 3) Ostwald ripening and octahedron growth. The detailed structural and morphological characterizations can be seen in Fig. S2.

In order to analyze the structure of the octahedral precursor, XRD was performed and the result is shown in Fig. S3. We can observe that the crystal phases of the precursor are very complex, mostly hydroxides and hydroxide carbonates. Thermogravimetric analysis (TGA) was performed to investigate the thermal behavior of the precursor. As shown in Fig. S4, there are two weight losses, the first weight loss of 15.27% below 200 °C and the second one of 30.89% between 200 and 380 °C. The first one is due to the loss of physical and chemical adsorbed water, and the later could be attributed to the inorganic substances like $CO3^{2-}$, which are the main components of the octahedral precursor. No weight loss over 380 °C are detected, suggesting that the precursor has transformed into $ZnCo_2O_4$ completely.

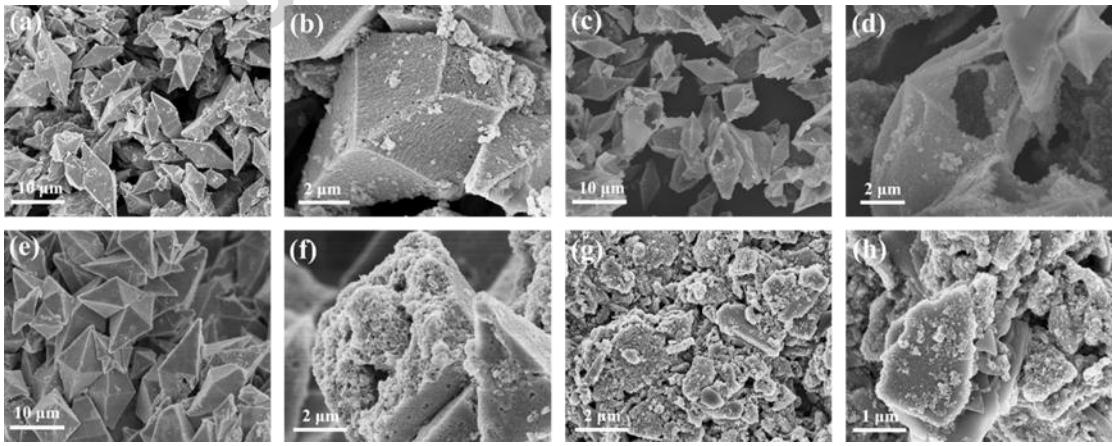

Fig. 2. SEM images of $ZnCo_2O_4$ with different interior structures. Solid (a, b), hollow (c, d), yolk-shell (e, f) and broken structures (g, h).

The thermal transformation process was performed at 600 °C with four different heating rates (1 °C/min, 2 °C/min, 3 °C/min and 5 °C/min). The corresponding products were collected and checked by SEM investigation, as shown in Fig. 2. At a ramping rate of 1 °C/min, the product obtained are solid octahedrons, which is designated as S-ZCO. The enlarged SEM image in Fig. S5b shows that S-ZCO is constituted by compactly stacked nanoparticles with particle size of about 10 nm. And many interparticle voids can be clearly observed, implying its porous feature. At a heating rate of 2 °C/min, well-defined hollow octahedrons (designated as H-ZCO) can be formed (Fig. 2c, d). The shells of these octahedrons are uniform and thin with an average thickness of 200 nm (Fig. S5c, d). Besides, they also consist of a large number of nanoparticles. When the heating rate increases to 3 °C/min, octahedral structure can still be well maintained with almost no broken octahedrons observed. Two typical views in Fig. 2f and Fig. S5e clearly demonstrate the yolk-shell architecture of the sample (designated as YS-ZCO). Besides, the shells possess large thickness of about 1 μm. At a high ramping rate of 5 °C/min, the obtained product presents an irregular morphology (see Fig. 2g, h), suggesting all the octahedrons are cracked or collapsed and transformed into broken structures (designated as B-ZCO).

In order to study the significance of the selection of appropriate Zn-Co precursor, the octahedral hydrothermal products of 3 hrs and 12 hrs were also employed as the annealing precursors. After heat treatment for 4 hrs at 600 °C with a heating rate of

2 °C /min, two products were obtained and their morphologies were examined by SEM as shown in Fig. S6. We can see that, for the precursor of 3 hrs, all the hollow octahedrons are broken after annealing, especially in the octahedral tip sites. While for the precursor of 12 hrs, the corresponding products are partly broken. This observation indicates a gradually increasing structural stability of precursors with increased hydrothermal reaction time. To further clarify this point, TGA curves of three samples were plotted (Fig. S7). With the increase of hydrothermal time, the thermal decomposition temperature of the three precursors gradually increases, which accords well with the above-mentioned judgement. These results demonstrate the significance of employing an appropriate solid precursor for acquiring well-defined anisotropic hollow architectures.

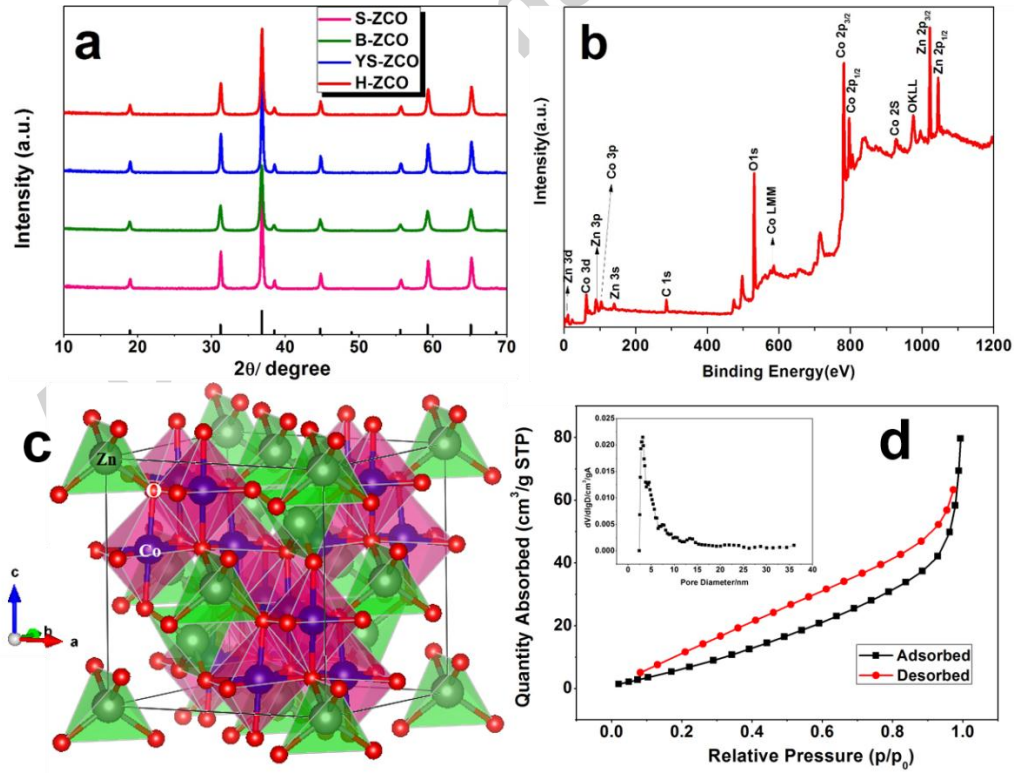

Fig. 3. (a) XRD patterns of as-prepared S-ZCO, H-ZCO, YS-ZCO, and B-ZCO; (b)

XPS spectra of the H-ZCO sample; (c) Crystal structure of spinel $ZnCo_2O_4$ and (d) Nitrogen adsorption–desorption isotherms and the corresponding pore size distributions (inset) of H-ZCO product.

The crystalline phase and component of the final products were examined by XRD patterns. As can be seen from Fig. 3a, all the diffraction peaks of the four samples match well with the values in standard $ZnCo_2O_4$ cubic spinel structure (PDF card NO. 23-1390, space group: Fd-3m (227), lattice constant a=8.095 Å). No other peaks of impurities were observed, verifying the high purity of the products. The XPS spectra of hollow octahedral $ZnCo_2O_4$ in Fig. 3b and Fig. S8 indicate the presence of Zn, Co and O elements and the absence of impurity. The schematic crystal structure of $ZnCo_2O_4$ is exhibited in Fig. 3c. It is a normal cubic spinel structure, with Zn ion occupying the tetrahedral sites and Co ions occupying the octahedral sites, which is isostructural to the structure of Co_3O_4. In order to explore the porosity properties of four samples (S-ZCO, H-ZCO, YS-ZCO, and B-ZCO), N_2 adsorption–desorption tests were carried out. The resulting adsorption–desorption isotherms and pore size distribution curves (see Fig. 3d and Fig. S9) demonstrate their mesoporous features. The porosity parameters are sumerized in Table S2. The H-ZCO and YS-ZCO exhibit relatively higher surface areas of 37.9, 35.9 $m^2 g^{-1}$ and pore volumes of 0.11, 0.15 $cm^3 g^{-1}$. The porous hollow structures not only offer increased interfacial contact sites between the electrolyte and active materials, but also provide large spaces to effectively buffer the repetitive volume changes, thus may improve the enhanced electrochemical performances of electrodes.

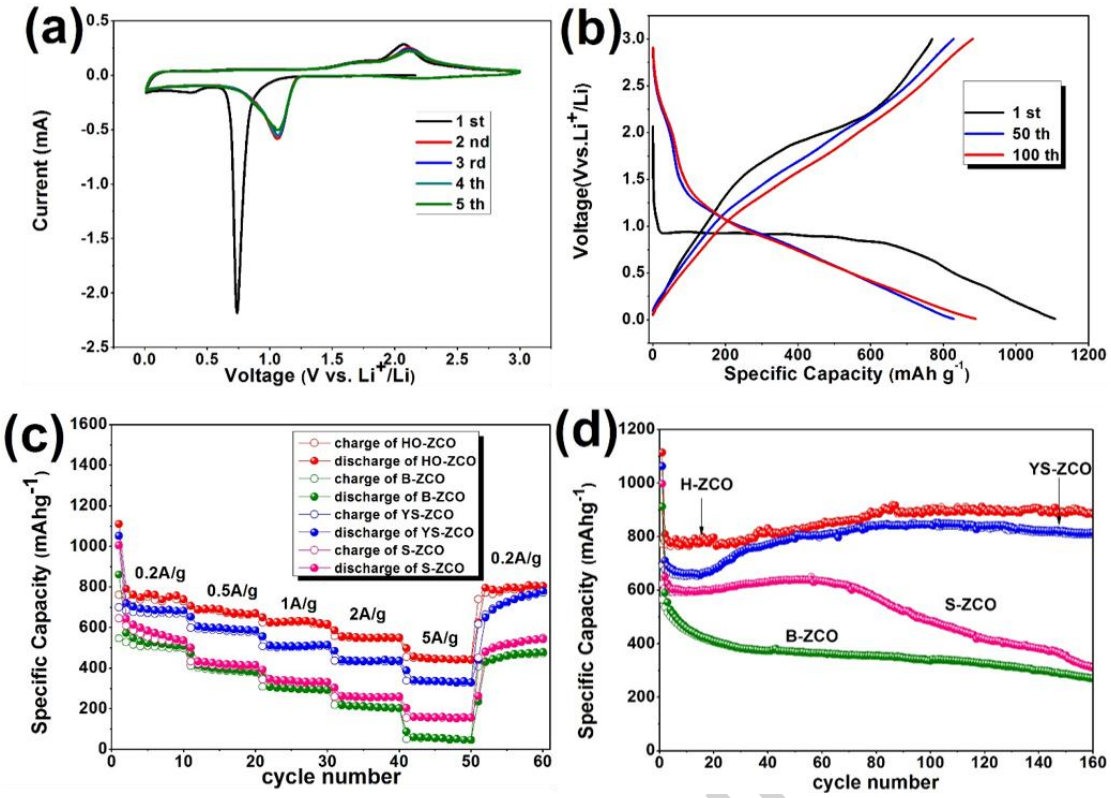

Fig. 4. (a) CV curves for H-ZCO at a scan rate of 0.1 mV s^{-1} in the potential range of 0.01 V to 3V; (b) Galvanostatic charge/discharge curves of H-ZCO anode at a current density of 0.2 A g^{-1}; (c) Specific capacities of four electrodes at various current densities from 0.2 A g^{-1} to 5 A g^{-1}; (d) Cycling performance of four electrodes at a current density of 0.2 A g^{-1};

The lithium-storage properties of the four samples were evaluated by assembling the standard $ZnCo_2O_4$/Li half batteries. Fig. 4a shows the CV curves of H-ZCO at a scan rate of 0.1 mV s^{-1} in the potential window of 0.01–3.0 V vs. Li/Li^+. We can observe that there is a large and sharp irreversible reduction peak centered at 0.67 V in the first cathodic process, corresponding to the reduction of $ZnCo_2O_4$ to Zn and Co,

accompanied with the formation of a solid electrolyte interphase (SEI). Meanwhile, there are two broad oxidation peaks located at 1.7 and 2.2 V in the first anodic process, which should be attributed to the oxidation of metallic Zn and Co to Zn^{2+} and Co^{3+}, respectively. For comparison, in the following scanning cycles, the cathodic peaks move to higher potential at around 1.1 V and become broader while the anodic peaks remain almost unchanged. These results indicate the different electrochemical reaction mechanisms from the irreversible reaction in the first discharge cycle [41]. It is worth mentioning that the CV curves are almost overlapped from the second cycle onwards, suggesting the excellent reversibility of the electrochemical reactions. Based on aforementioned analysis, the electrochemical reactions of the as-prepared hollow octahedral $ZnCo_2O_4$ can be clarified as follows [8, 41-43]:

$$ZnCo_2O_4+8Li^++8e^-\rightarrow Zn+2Co+4Li_2O \quad (1)$$

$$Zn+ Li^++e^-\rightarrow ZnLi \quad (2)$$

$$Zn+Li_2O\leftrightarrow ZnO+2Li^++2e^- \quad (3)$$

$$2Co+2\ Li_2O\leftrightarrow 2CoO+4Li^++4e^- \quad (4)$$

$$2CoO+2/3\ Li_2O\leftrightarrow 2/3Co_3O_4+4/3Li^++4/3e^- \quad (5)$$

Fig. 4b displays representative galvanostatic charge/discharge profiles of H-ZCO in a potential window of 0.01 to 3 V at a current rate of 0.2 A g^{-1}. As delivered in the curves, the initial discharge and charge capacities are 1110 mA h g^{-1} and 771 mA h g^{-1} respectively, corresponding to a moderate coulombic efficiency of 70%. The irreversible capacity loss can be mainly ascribed to the formation of solid electrolyte

interphase (SEI) [44, 45]. As to the 50^{th} and 100^{th} cycles, they deliver a high coulombic efficiency of nearly 100%, which indicates the superior reversibility and cycling stability of H-ZCO electrode.

The rate performance is another important merit for LIBs due to increasing demand for high-power energy storage systems. Here the specific capacities at various current densities were evaluated (Fig. 4c). We can see that the hollow and yolk-shell structures show better rate performances than S-ZCO. H-ZCO anode delivers discharge capacities of 760, 680, 626, 558 and 456 mA h g^{-1} when the current density increases from 0.2, 0.5, 1, 2 to 5 A g^{-1}, respectively. For YS-HCO anode, the corresponding specific capacities are 700, 590, 507, 435 and 337 mA h g^{-1}, respectively. When the current density returns to 0.2 A g^{-1}, the specific capacity of H-ZCO and YS-ZCO can recover to 804 and 780 mA h g^{-1}, respectively, which are a little higher than their initial capacities at 0.2 A g^{-1}. For comparison, S-ZCO anode only maintains a low specific capacity of 155 mA h g^{-1} at 5 A g^{-1}, suggesting the great advantage of the hollow architectures. It is notable that H-ZCO shows a large capacity retention of 60% even at a high current density of 5 A g^{-1}, demonstrating its great potential for application in high-power LIBs. This good rate performance also outperforms those in reported literatures with similar hollow structures [16, 30, 35, 36, 46] (see Table S3). In order to better understand the good rate performance of H-ZCO anode, electrochemical impedance spectra (EIS) were evaluated and the resulting Nyquist plots are shown in Fig. S10. It can be observed that four Nyquist plots are similar to each other in the shape, with a semicircle in the high- and

medium-frequency regions and a straight line in the low-frequency region. The semicircles of four samples in middle frequency range are related to the charge-transfer process and their diameters indicate the interfacial charge transfer resistance. The straight lines in the low-frequency range should be ascribed to the solid-state diffusion of Li^+ in the electrode materials [45, 47]. The semicircle diameters in Nyquist plots of H-ZCO and YS-ZCO are very near but obviously much smaller than those of S-ZCO and B-ZCO, implying their lower charge-transfer impedances. Besides, at low-frequency range, the H-ZCO presents a higher slope compared to the YS-ZCO electrode, suggesting faster Li^+ diffusion rate of the porous hollow structure. This shows that the electrons and ions can transfer more freely in the H-ZCO electrode and therefore leads to its outstanding rate performance.

Fig. 4d depicts the cycling performance of four electrodes at a current density of 0.2 A g^{-1}. It can be clearly observed that B-ZCO anode shows quite poor cycling capability. The specific capacity displays a sharp decline in the initial 20 cycles and it only maintains quite low capacity of 270 mA h g^{-1} after 160 cycles. While the other three samples (S-ZCO, H-ZCO, YS-ZCO) do not suffer severe capacity fading in the initial cycles, which indicates the higher stability of the octahedral micro-/nanostructures. Besides, we can also see that H-ZCO and YS-ZCO electrodes exhibit much better cycling stability than the S-ZCO electrode. The capacities of H-ZCO and YS-ZCO decrease slightly in the initial 20 cycles, which can be ascribed to the formation of unstable SEI layer [48]. After that they experience an upward trend and finally maintain at 880 and 845 mA h g^{-1} after 160 cycles respectively, with

capacity retentions of 112.7% and 124.8% based on the second reversible capacity. These cycling stabilities are among the best in comparison with reported literatures (see Table S3). Besides, the phenomenon of capacity increase with cycling is very common in many metal oxides anode, which can be ascribed to the reversible formation/dissolution of the polymer/gel-like film on the surface of the active materials during the discharge/charge cycles [10, 49-51]. Ex-situ SEM measurements were conducted to confirm the mechanical stability of the hollow micro-/nanostructures of H-ZCO and YS-ZCO. The morphologies of the electrodes after 100 cycles are shown in Fig. S12 and Fig. S13. They can still remain the integrity of octahedral structures to a great extent. To further evaluate the high-rate cycling stability of four anodes, continuous charge/discharge at 1 A g^{-1} were performed for 300 cycles (see Fig. S11). The H-ZCO anode still exhibits the best cycling performance with a capacity retention of 96.4% based on the reversible capacity of the second cycle. These analyses suggest that the porous hollow architectures can provide extra space to promote lithium ion diffusion and accommodate the volume variation during cycling. This again demonstrates its great potential as promising high-rate and stable anode for next-generation LIBs.

3. Conclusion

In summary, well-defined octahedral $ZnCo_2O_4$ with solid, hollow and yolk-shell micro-/nanostructures were firstly constructed via citrate-assisted hydrothermal synthesis and subsequent controlled annealing method. We found several key parameters that affect the process. First, citrate content plays an important role in the

formation of octahedral Zn-Co-precursor. Second, the thermal stability of Zn-Co-precursor is crucial for well preserving the octahedral morphology during pyrolysis. Third, the annealing rate decides the interior structure of $ZnCo_2O_4$ micro-octahedrons. When evaluated as LIB anodes, H-ZCO shows the best lithium storage properties due to its abundant electrochemically active sites, smooth ion diffusion channels as well as good structural stability. It exhibits high discharge capacities of 880 mA h g^{-1} over 160 cycles at 0.2 A g^{-1}, 650 mA h g^{-1} over 300 cycles at 1 A g^{-1} as well as 60% capacity retention even at a high current density of 5 A g^{-1}. The facile, scalable synthesis and excellent electrochemical performance render the hollow $ZnCo_2O_4$ micro-octahedron very promising as next-generation LIB anode.

Acknowledgements

This work was supported by National Key Basic Research Program of China (No. 2014CB932400), Joint Fund of the National Natural Science Foundation of China and the China Academy of Engineering Physics (Nos. U1330123 and U1401243), National Nature Science Foundation of China (No. 51232005), Shenzhen Technical Plan Project (JCYJ 20150529164918735).

References

[1] P. Poizot, S. Laruelle, S. Grugeon, L. Dupont, J. Tarascon, Nature, 407 (2000) 496-499.

[2] J. Wu, X. Qin, C. Miao, Y.-B. He, G. Liang, D. Zhou, M. Liu, C. Han, B. Li, F. Kang, Carbon, 98 (2016) 582-591.

[3] C. Han, Y.-B. He, S. Wang, C. Wang, H. Du, X. Qin, Z. Lin, B. Li, F. Kang, ACS

Appl. Mater. Interfaces, 8 (2016) 18788-18796.

[4] C. Miao, M. Liu, Y.-B. He, X. Qin, L. Tang, B. Huang, R. Li, B. Li, F. Kang, Energy Storage Materials, 3 (2016) 98-105.

[5] W. Li, X. Guo, Y. Lu, L. Wang, A. Fan, M. Sui, H. Yu, Energy Storage Materials, 7 (2017) 203-208.

[6] H. Buqa, D. Goers, M. Holzapfel, M.E. Spahr, P. Novák, J. Electrochem. Soc., 152 (2005) A474-A481.

[7] H. Wang, M. Yoshio, J. Power Sources, 93 (2001) 123-129.

[8] J. Bai, X. Li, G. Liu, Y. Qian, S. Xiong, Adv. Funct. Mater., 24 (2014) 3012-3020.

[9] H. Chen, Q. Zhang, J. Wang, Q. Wang, X. Zhou, X. Li, Y. Yang, K. Zhang, Nano Energy, 10 (2014) 245-258.

[10] J. Deng, X. Yu, Y. He, B. Li, Q.-H. Yang, F. Kang, Energy Storage Materials, 6 (2017) 61-69.

[11] G. Huang, Q. Li, D. Yin, L. Wang, Adv. Funct. Mater., 27 (2017) 1604941.

[12] Y. Zhao, X. Li, B. Yan, D. Xiong, D. Li, S. Lawes, X. Sun, Adv. Energy Mater., 6 (2016) 1502175.

[13] S.H. Choi, Y.C. Kang, ChemSusChem, 6 (2013) 2111-2116.

[14] Q. Xie, F. Li, H. Guo, L. Wang, Y. Chen, G. Yue, D.-L. Peng, ACS Appl. Mater. Interfaces, 5 (2013) 5508-5517.

[15] L. Yu, L. Zhang, H.B. Wu, G. Zhang, X.W.D. Lou, Energy Environ. Sci., 6 (2013) 2664-2671.

[16] J. Li, J. Wang, D. Wexler, D. Shi, J. Liang, H. Liu, S. Xiong, Y. Qian, J. Mater.

Chem. A, 1 (2013) 15292-15299.

[17] L. Guo, Q. Ru, X. Song, S. Hu, Y. Mo, J. Mater. Chem. A, 3 (2015) 8683-8692.

[18] J.B. Joo, Q. Zhang, M. Dahl, I. Lee, J. Goebl, F. Zaera, Y. Yin, Energy Environ. Sci., 5 (2012) 6321-6327.

[19] C.-C. Huang, W. Huang, C.-S. Yeh, Biomaterials, 32 (2011) 556-564.

[20] H. Ren, J. Sun, R. Yu, M. Yang, L. Gu, P. Liu, H. Zhao, D. Kisailus, D. Wang, Chem. Sci., 7 (2016) 793-798.

[21] B. Wang, J.S. Chen, H.B. Wu, Z. Wang, X.W. Lou, J. Am. Chem. Soc., 133 (2011) 17146-17148.

[22] Q. Zhao, Y. Gao, X. Bai, C. Wu, Y. Xie, Eur. J. Inorg. Chem., 2006 (2006) 1643-1648.

[23] C. Deng, H. Hu, X. Ge, C. Han, D. Zhao, G. Shao, Ultrasoni. Sonochem., 18 (2011) 932-937.

[24] L. Cao, D. Chen, R.A. Caruso, Angew. Chem., Int. Ed., 52 (2013) 10986-10991.

[25] S.E. Skrabalak, L. Au, X. Li, Y. Xia, Nat. protoc., 2 (2007) 2182-2190.

[26] H. Xu, W. Wang, Angew. Chem., Int. Ed., 46 (2007) 1489-1492.

[27] J. Wang, N. Yang, H. Tang, Z. Dong, Q. Jin, M. Yang, D. Kisailus, H. Zhao, Z. Tang, D. Wang, Angew. Chem., Int. Ed.,, 125 (2013) 6545-6548.

[28] Z. Dong, H. Ren, C.M. Hessel, J. Wang, R. Yu, Q. Jin, M. Yang, Z. Hu, Y. Chen, Z. Tang, Adv. Mater., 26 (2014) 905-909.

[29] X. Wang, M. Liao, Y. Zhong, J.Y. Zheng, W. Tian, T. Zhai, C. Zhi, Y. Ma, J. Yao, Y. Bando, Adv. Mater., 24 (2012) 3421-3425.

[30] L. Zhou, D. Zhao, X.W. Lou, Adv. Mater., 24 (2012) 745-748.

[31] G. Zhang, L. Yu, H.B. Wu, H.E. Hoster, X.W.D. Lou, Adv. Mater., 24 (2012) 4609-4613.

[32] O. Shchepelina, V. Kozlovskaya, S. Singamaneni, E. Kharlampieva, V.V. Tsukruk, J. Mater. Chem., 20 (2010) 6587-6603.

[33] L. Zhang, H.B. Wu, S. Madhavi, H.H. Hng, X.W. Lou, J. Am. Chem. Soc., 134 (2012) 17388-17391.

[34] R. Wu, X. Qian, F. Yu, H. Liu, K. Zhou, J. Wei, Y. Huang, J. Mater. Chem. A, 1 (2013) 11126-11129.

[35] R. Wu, X. Qian, X. Rui, H. Liu, B. Yadian, K. Zhou, J. Wei, Q. Yan, X.Q. Feng, Y. Long, Small, 10 (2014) 1932-1938.

[36] R. Wu, X. Qian, K. Zhou, J. Wei, J. Lou, P.M. Ajayan, ACS Nano, 8 (2014) 6297-6303.

[37] Y. Yin, R.M. Rioux, C.K. Erdonmez, S. Hughes, G.A. Somorjai, A.P. Alivisatos, Science, 304 (2004) 711-714.

[38] J. Li, J. Wang, X. Liang, Z. Zhang, H. Liu, Y. Qian, S. Xiong, ACS Appl. Mater. Interfaces, 6 (2013) 24-30.

[39] A.J. Pedersen, J. Hazard. Mater., 95 (2002) 185-198.

[40] N. Kotsakis, C. Raptopoulou, V. Tangoulis, A. Terzis, J. Giapintzakis, T. Jakusch, T. Kiss, A. Salifoglou, Inorg.Chem., 42 (2003) 22-31.

[41] Y. Zhu, C. Cao, J. Zhang, X. Xu, J. Mater. Chem. A, 3 (2015) 9556-9564.

[42] S. Hao, B. Zhang, S. Ball, M. Copley, Z. Xu, M. Srinivasan, K. Zhou, S.

Mhaisalkar, Y. Huang, J. Power Sources, 294 (2015) 112-119.

[43] G. Gao, H.B. Wu, B. Dong, S. Ding, X.W.D. Lou, Adv. Sci., 2 (2015) 1400014.

[44] B. Jiang, C. Han, B. Li, Y. He, Z. Lin, ACS Nano, 10 (2016) 2728-2735.

[45] J. Li, S. Xiong, Y. Liu, Z. Ju, Y. Qian, ACS Appl. Mater. Interfaces, 5 (2013) 981-988.

[46] L. Huang, G.H. Waller, Y. Ding, D. Chen, D. Ding, P. Xi, Z.L. Wang, M. Liu, Nano Energy, 11 (2015) 64-70.

[47] A.K. Mondal, D. Su, S. Chen, X. Xie, G. Wang, ACS Appl. Mater. Interfaces, 6 (2014) 14827-14835.

[48] H. Sun, G. Xin, T. Hu, M. Yu, D. Shao, X. Sun, J. Lian, Nat. Commun., 5 (2014) 4526.

[49] S. Grugeon, S. Laruelle, L. Dupont, J.-M. Tarascon, Solid State Sci., 5 (2003) 895-904.

[50] L. Li, K.H. Seng, Z. Chen, Z. Guo, H.K. Liu, Nanoscale, 5 (2013) 1922-1928.

[51] X. Li, L. Qiao, D. Li, X. Wang, W. Xie, D. He, J. Mater. Chem. A, 1 (2013) 6400-6406.